

Fast Lithography Simulation under Focus Variations for OPC and Layout Optimizations

Peng Yu^a, David Z. Pan^a and Chris A. Mack^{a,b}

^aElectrical and Computer Engineering Department, University of Texas at Austin

^bChemical Engineering Department, University of Texas at Austin

ABSTRACT

In 90nm technology and beyond, process variations should be considered such that the design will be robust with respect to process variations. Focus error and exposure dose variations are the two most important lithography process variations. In a simple approximation, the critical dimension (CD) is about linearly related to the exposure dose variation, while it is quadratically related to the focus variation. Other kinds of variations can be reduced to these variations effectively as long as they are small. As a metric to measure the effects of exposure dose variations, normalized image log-slope (NILS) is pretty fast to compute once we have the aerial images. OPC software has used it as an optimization objective. But focus variation has not been commonly considered in current OPC software. One way is to compute several aerial images at different defocus conditions, but this approach is very time consuming.

In this paper, we derive an analytical formula to compute the aerial image under any defocus condition. This method works for any illumination scheme and is applicable to both binary and phase shift masks (PSM). A model calibration method is also provided. It is demonstrated that there is only about 2-3x runtime increase using our fast focus-variational lithography simulation compared to the current single-focus lithography simulation. To confirm the accuracy, our model is compared with PROLITHTM. This ultra-fast simulator can enable better and faster process-variation aware OPC to make layouts more robust under process variations, and directly guide litho-aware layout optimizations.

Keywords: Model Based OPC, Process Variation, Depth-of-Focus, Fast Lithography Simulation

1. INTRODUCTION

Traditional model-based OPC uses phenomenological lithography models calibrated under nominal process conditions. The variable threshold resist model family was introduced and better fitting parameters have been proposed to increase the accuracy of the model predictions.¹⁻⁵ However, as lithography systems print higher densities and finer dimensions, process windows are reduced, while the CD sensitivities to process variations are increased. Thus, it is not enough to use only the nominal lithography process conditions. Fast and accurate variational lithography modeling is demanding.

Some attempts have been made to incorporate the lithography process variation awareness into OPC software. For example, defocus aerial images, instead of in-focus aerial image, have been used in OPC software to improve process window robustness.^{6,7} But they rely on extensive lithography simulations to choose the appropriate defocus value, which is very expensive. Image-log slope, as an indicator of process sensitivity to dose variations, has also been proposed.^{6,8} But this approach is incapable of handling focus variations. None of these attempts are capable of giving the full information of the process window. Due to prohibitive runtimes of lithography simulations, it is simply impossible to simulate across the entire process window without extensive compute power. In fact, even without consideration of the process window, it has been reported that model-based OPC software could run for days on multiple computers for a single design.⁹

Further author information: (Send correspondence to David Z. Pan)

Peng Yu: E-mail: yupeng@cerc.utexas.edu

David Z. Pan: E-mail: dpan@ece.utexas.edu, Telephone: +1 (512) 471-1436

Chris A. Mack: E-mail: chris@lithoguru.com

Focus Exposure Matrix (FEM) shows the variation of linewidth as a function of focus error and exposure energy.¹⁰ Traditionally, it requires a lot of simulations (in the order of hundred) to get the FEM at a given location, which is time-consuming. It is observed that the FEM can be fitted by a polynomial,¹¹

$$\text{CD} = \text{CD}_0 + (a_0 + a_1 z^2 + a_2 z^4)(b_0(I - I_0) + b_1(I - I_0)^3), \quad (1)$$

where I is the intensity threshold, I_0 is the iso-focal intensity threshold, CD_0 is the CD measured at iso-focal threshold and zero focus error, z is the focus error and a_i and b_i are fitting parameters. (1) also suggest that there must be some physical meaning of these parameters — the aerial image can be expanded with respect to focus error z . Based on this idea, we proposes a variational lithography modeling (VLIM) for the first time, to our best knowledge. The main contributions are as follows.

- We derive a new analytical defocus aerial image expansion, which can generically handle any focus variation and illumination scheme.
- The accuracy of VLIM is confirmed.
- The runtime of our VLIM is only about $2 \sim 3 \times$ that of the non-variational LIM due to the analytical nature of our models. It is fast enough to use it to use it in OPC softwares.

The rest of the paper is organized as follows. Section 2 presents our analytical variational lithography modeling. Section 3 shows the experimental results, followed by conclusions in section 4.

2. VARIATIONAL LITHOGRAPHY MODEL (VLIM)

Traditional phenomenological lithography simulators (used in various OPC softwares) can be decomposed into aerial image simulators and photoresist simulators, which compute the print contours based on the aerial images.

In this section, a new variational lithography model is proposed. In particular, an analytical formula for the aerial image at any defocus condition is derived. The impact of dose variation on the printed contour can be handled easily once the defocus aerial image is computed.

2.1. Optics Preliminary — Hopkins Equation

The aerial image can be described by the *Hopkins Equation*¹²

$$\mathcal{J}(f, g) = \iint \mathcal{T}(f' + f, g' + g; f', g') \mathcal{F}(f' + f, g' + g) \mathcal{F}^*(f', g') df' dg'. \quad (2)$$

$\mathcal{J}(f, g)$ is the inverse Fourier transforms of the aerial image intensity $I(x, y)$, where (f, g) denotes a point in the frequency domain and (x, y) denotes a point in the object plane. $\mathcal{F}(f, g)$ is the inverse Fourier transforms of the mask transmission function $F(x, y)$. $\mathcal{T}(f', g'; f'', g'')$ is called the *transmission cross coefficient* (TCC), given by

$$\mathcal{T}(f', g'; f'', g'') = \iint \mathcal{J}_O^-(f, g) \mathcal{K}(f + f', g + g') \mathcal{K}^*(f + f'', g + g'') df dg, \quad (3)$$

where $\mathcal{J}_O^-(f, g)$ and $\mathcal{K}(f, g)$ are the illumination function and the projection system transfer function, respectively. Denoting the focal error as z and supposing the shape of the pupil is a circle (without loss of generality), $\mathcal{K}(f, g)$ can be written as

$$\mathcal{K}(f, g) = \mathcal{K}_0(f, g) e^{i\pi z(f^2 + g^2)}, \quad (4)$$

where

$$\mathcal{K}_0(f, g) = \begin{cases} 1 & f^2 + g^2 < 1 \\ 0 & f^2 + g^2 > 1 \end{cases}. \quad (5)$$

For conventional illumination with *partially coherent factor* s , $\mathcal{J}_O^-(f, g)$ is written as

$$\mathcal{J}_O^-(f, g) = \begin{cases} \frac{1}{\pi s^2} & f^2 + g^2 < s^2 \\ 0 & f^2 + g^2 > s^2 \end{cases}. \quad (6)$$

Other illuminations can be described similarly. By Fourier transforming $\mathcal{J}(f, g)$ in (3), we get the aerial image intensity $I(x, y)$.

2.2. Variational Aerial Image Modeling

In this section, we derived our new analytical variational aerial image model. We adapt and extend the moment expansion method¹³ (which only handles fully coherent illumination) to compute defocus aerial image for arbitrary illumination schemes.

Expanding $e^{i\pi z(f^2+g^2)}$ as $\sum_{n=0}^{\infty} \frac{(i\pi z(f^2+g^2))^n}{n!}$, plugging it in (3) and using Binomial Expansion, we have (7)

$$\begin{aligned} \mathcal{T}(f', g'; f'', g'') &= \sum_{n=0}^{\infty} \frac{(i\pi z)^n}{n!} \sum_{k=0}^n \binom{n}{k} \iint \left((f+f')^2 + (g+g')^2 \right)^k \left(- \left((f+f'')^2 + (g+g'')^2 \right) \right)^{n-k} \\ &\quad \times \mathcal{J}_{\mathcal{O}}^-(f, g) \mathcal{K}_0(f+f', g+g') \mathcal{K}_0^*(f+f'', g+g'') df dg. \end{aligned} \quad (7)$$

That is, $\mathcal{T}(f', g'; f'', g'')$ can be expanded as

$$\mathcal{T}(f', g'; f'', g'') = \sum_{n=0}^{\infty} z^n \mathcal{T}_n(f', g'; f'', g''). \quad (8)$$

Plug (8) into (2), we end up with the following form

$$\mathcal{J}(f, g) = \sum_{n=0}^{\infty} z^n \mathcal{J}_n(f, g), \quad (9)$$

where

$$\mathcal{J}_n(f, g) = \iint \mathcal{T}_n(f'+f, g'+g; f', g') \mathcal{F}(f'+f, g'+g) \mathcal{F}^*(f', g') df' dg', \quad (10)$$

$$\mathcal{T}_n(f', g'; f'', g'') = \frac{(-i\pi)^n}{n!} \sum_{k=0}^n \binom{n}{k} (-1)^k \mathcal{T}_{n,k}(f', g'; f'', g''), \quad (11)$$

and

$$\begin{aligned} \mathcal{T}_{n,k}(f', g'; f'', g'') &= \iint \left((f+f')^2 + (g+g')^2 \right)^k \left((f+f'')^2 + (g+g'')^2 \right)^{n-k} \\ &\quad \times \mathcal{J}_{\mathcal{O}}^-(f, g) \mathcal{K}_0(f+f', g+g') \mathcal{K}_0^*(f+f'', g+g'') df dg. \end{aligned} \quad (12)$$

By Fourier transforming (9), we have the aerial intensity

$$I(x, y) = \sum_{n=0}^{\infty} z^n I_n(x, y). \quad (13)$$

Note that $\mathcal{T}_{n,k}$ satisfies

$$\begin{aligned} \mathcal{T}_{n,k}(f', g'; f'', g'') &= \iint \mathcal{J}_{\mathcal{O}}^-(f, g) \mathcal{K}_k(f+f', g+g') \mathcal{K}_{n-k}^*(f+f'', g+g'') df dg \\ &= \iint \mathcal{J}_{\mathcal{O}}^{-*}(f, g) \mathcal{K}_{n-k}^*(f+f'', g+g'') \mathcal{K}_k(f+f', g+g') df dg \\ &= \mathcal{T}_{n, n-k}^*(f'', g''; f', g'). \end{aligned} \quad (14)$$

For binary mask or phase-shift mask (PSM) with phase 0° and 180° , since the mask transmission function $F(x, y)$ is always real, we have

$$\mathcal{F}(f, g) = \mathcal{F}^*(-f, -g), \quad (15)$$

where $\mathcal{F}(f, g)$ is the mask transmission function $F(x, y)$ in Fourier space.

The aerial image $I(x, y)$ is always real, so are its expansions — $I_n(f, g)$'s. Similar to (15), we have

$$\mathcal{J}_n(f, g) = \mathcal{J}_n^*(-f, -g). \quad (16)$$

By using (14) and (15) and, we have

$$\begin{aligned} & \iint \mathcal{J}_{n, n-k}(f' + f, g' + g; f', g') \mathcal{F}(f' + f, g' + g) \mathcal{F}^*(f', g') df' dg' \\ &= \left(\iint \mathcal{J}_{n, k}(f' - f, g' - g; f', g') \mathcal{F}(f' - f, g' - g) \mathcal{F}^*(f', g') df' dg' \right)^* \end{aligned} \quad (17)$$

If n is odd, it is easily seen that

$$\mathcal{J}_n(f, g) = -\mathcal{J}_n^*(-f, -g). \quad (18)$$

From (16) and (18), we have $\mathcal{J}_n(f, g) = 0$ for odd n 's. Finally, we have the *defocus aerial image expansion* (less terms are presented comparing with (13)),

$$I(x, y) = \sum_{n=0}^{\infty} z^{2n} I_{2n}(x, y). \quad (19)$$

$I_{2n}(x, y)$'s are called the *variational aerial images*, and the corresponding $\mathcal{J}_{2n}(f', g'; f'', g'')$'s are called the *variational TCCs*.

It is easy to see that I_0 is the in-focus ($z = 0$) aerial image. (19) tells us that the defocus aerial image can be expressed as the in-focus image plus some correction terms. Supposing that the focus error range is so small such that the third term and higher order terms in (19) can be ignored, we have a simple formula for the defocus aerial image intensity

$$I(x, y; z) \cong I_0(x, y) + z^2 I_2(x, y). \quad (20)$$

Higher order terms in (19) can be retained when the aerial images at a bigger focus error range are interested. Because the aerial image intensity is a function of focus error, we add the focus error z back to the left hand side of (20), which was previously omitted for the notation simplicity.

2.3. The Look-up Table Method and the Error Bound

The aerial image $I(x, y)$ (associated with (2)) and the variational aerial images $I_{2n}(x, y)$ in (19) are computed by the look-up table method.¹⁴ By decomposing the TCC and the variational TCCs, the kernels are computed and stored in these tables. As an example, say TCC is decomposed into

$$\mathcal{J}(f', g'; f'', g'') = \sum_{k=0}^{\infty} \alpha_k \phi_k(f', g') \phi_k^*(f'', g'') \quad (21)$$

it was stated that the worst case error in the image ($I(x, y)$) can be uniformly bounded by $\text{EB}(m) = \sum_{k=m}^{\infty} |\alpha_k|^2$, if the first m kernels are used.¹⁵ The error bound for $I_{2n}(x, y)$ can be determined similarly.

3. EXPERIMENTAL RESULTS

3.1. The Accuracies of the Aerial Image Simulator and the Variational Aerial Image Simulator

In order to verify (20), we implement the aerial image simulator (AIS) (computing $I(x, y; z)$ based on TCC) and the variational aerial image simulator (VAIS) (computing $I_{2n}(x, y)$ based on the variational TCCs) in C++.

Since their implementations are almost the same except that different functions are used (like $e^{i\pi z(f^2+g^2)}$ in (4) versus $((f+f')^2+(g+g')^2)^k$ in (12)), the accuracy confirmation of AIS indicates the accuracy of VAIS.

Because the periodic patterns have the exact analytical aerial image intensity solutions (no aberrations, circular source shape and exit pupil), we test the accuracy of AIS on a special case — the lines and spaces pattern. For a 1D periodic pattern with the period p , the mask transmission coefficient in the frequency domain is described by

$$\mathcal{F}(f, g) = a_n \sum_{n=-\infty}^{\infty} \delta(f - \frac{n}{p}, g). \quad (22)$$

The aerial image intensity is

$$\begin{aligned} I(x, y) &= \sum_{m, n=-\infty}^{\infty} a_m a_n \iint df dg e^{-2\pi i(fx+gy)} \iint df' dg' \mathcal{T}(f' + f, g' + g; f', g') \delta(f' + f - \frac{m}{p}, g' + g) \delta(f' - \frac{n}{p}, g') \\ &= \sum_{m, n=-\infty}^{\infty} a_m a_n \iint df' dg' \delta(f' - \frac{n}{p}, g') \iint df dg e^{-2\pi i(fx+gy)} \mathcal{T}(f' + f, g' + g; f', g') \delta(f' + f - \frac{m}{p}, g' + g) \\ &= \sum_{m, n=-\infty}^{\infty} a_m a_n \iint df' dg' \delta(f' - \frac{n}{p}, g') e^{-2\pi i((\frac{m}{p}-f')x+(-g')y)} \mathcal{T}(\frac{m}{p}, 0; f', g') \\ &= \sum_{m, n=-\infty}^{\infty} a_m a_n \mathcal{T}(\frac{m}{p}, 0; \frac{n}{p}, 0) e^{-2\pi i(m-n)\frac{x}{p}} \end{aligned} \quad (23)$$

$\mathcal{T}(\frac{m}{p}, 0; \frac{n}{p}, 0)$ is zero for $\frac{|m-n|}{p} \geq 2$ or $\frac{|n|}{p} \geq 1+s$ or $\frac{|m|}{p} \geq 1+s$. E.C. Kintner¹⁶ showed the exact analytical solution of the special TCC case ($\mathcal{T}(f', 0; f'', 0)$) for a partially coherent source without aberrations. So the exact analytical solution of the aerial image intensity is

$$I(x, y) = \sum_{\substack{|m-n| < 2p \\ |n| < (1+s)p \\ |m| < (1+s)p}} a_m a_n \mathcal{T}(\frac{m}{p}, 0; \frac{n}{p}, 0) e^{-2\pi i(m-n)\frac{x}{p}} \quad (24)$$

By (24), we compute the aerial image intensity at the space edge $I|_{\text{edge}} = 0.302363$ for a periodic 100nm space pattern on a 200nm pitch, with the conventional partially coherent illumination ($s = 0.7$), the wave length $\lambda = 193\text{nm}$ and the numerical aperture $\text{NA} = 0.8$. Figure 1 shows the image CD error ($I|_{\text{edge}}$ is the intensity threshold) as a function of the simulation grid step size. The source grid size is the step size used to numerically compute the integral in (3). All kernels and the maximum support region are used in AIS to drive the accuracy to the full extent. The trend shows that the error of AIS converge to zero as the source grid size goes to zero. And its accuracy is comparable to that of PROLITHTM.

Although the comparison is made only for AIS at $z = 0$, we believe AIS and VAIS are accurate (with all kernels and the maximum support region) when the grid size is small enough.

3.2. Defocus Aerial Image Expansion Verification

To verify the defocus aerial image expansion method, we ran PROLITHTM simulations with the same optical parameters as those in the previous subsection. Figure 2 shows the relative aerial image intensity as a function of the focus error z at several randomly chosen locations on a Five Bar pattern (width 100nm, pitch 200nm) simulated by PROLITHTM. Each location corresponds to one kind of symbol in Figure 2. All the curves are symmetric about $z = 0\text{nm}$, which confirms that no odd terms are presented in (19). Figure 3 shows the aerial image intensity as a function of focus error z is approximately parabolas within the range of $-200\text{nm} \sim 200\text{nm}$. Dotted data are from PROLITHTM simulations. The curves are the parabolas fitted to the data within this range.

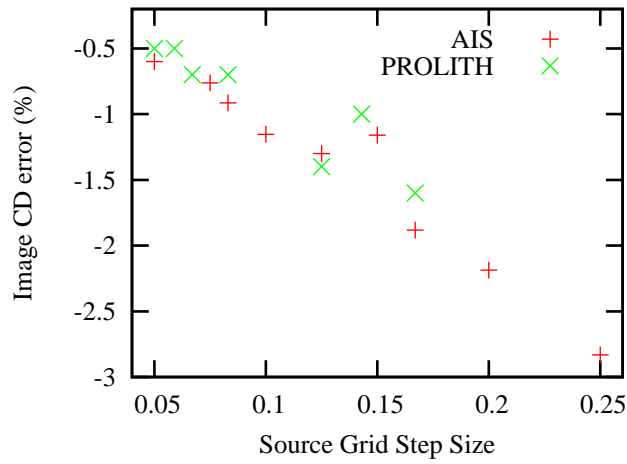


Figure 1. Aerial image CD errors simulated by PROLITHTM and AIS. The aerial image CD error converges to zero when the grid step size goes to zero for both PROLITHTM and AIS. The result of AIS and PROLITHTM is comparable.

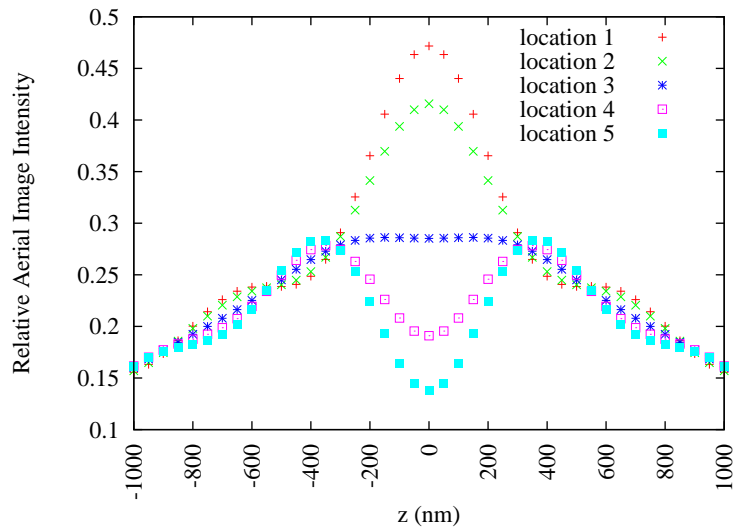


Figure 2. Aerial image intensity simulation results (PROLITHTM) at 5 randomly chosen locations.

Figure 4 shows $I|_{z=z_0} - I|_{z=0}$, $I_2z_0^2$, $I_4z_0^4$, $I_2z_1^2$ and $I_4z_1^4$ of the same Five Bar pattern ($z_0 = 100\text{nm}$, $z_1 = 200\text{nm}$). $I_4z_0^4$ can be ignored because it is much smaller than $I_2z_0^2$ ($z_0 = 100\text{nm}$). For $z_1 = 200\text{nm}$, $I_2z_1^2$ is still about 5 times $I_4z_1^4$. Let us say the criterion is $I_4z_1^4$ can be ignore if it is smaller than one fifth of $I_2z_1^2$. Then the approximation in (20) is appropriate within $\pm 200\text{nm}$.

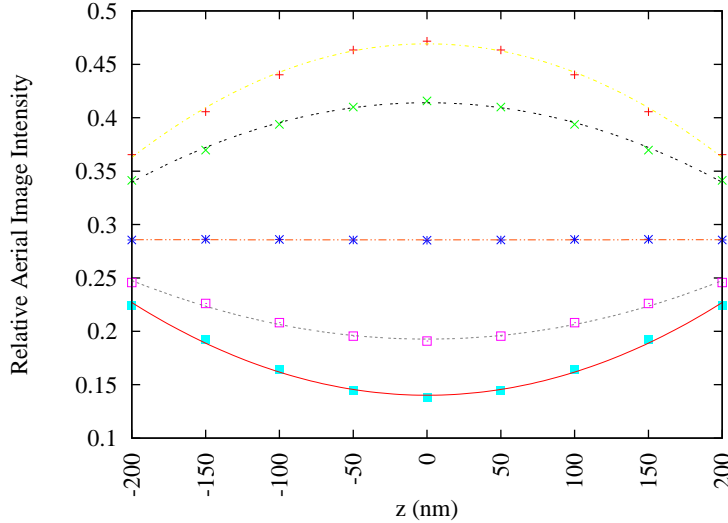


Figure 3. Parabola behavior of the aerial image intensity curves at 5 randomly chosen locations. The focus error range is between -200 nm and 200 nm. Dotted data are from PROLITHTM simulations. The curves are the data fitted parabolas within this range.

3.3. Runtime Comparison

Table 1 shows the runtime of computing the defocus aerial images (at a single focus error z_1) by computing I directly and by computing I_0 and I_2 . The look-up table method is used to compute I , I_0 and I_2 . The same number of kernels were used. To be conservative, we may want to use one time more kernels in I_2 than in I_0 . So the runtime of the second method is about $2 \sim 3\times$ that of the first method.

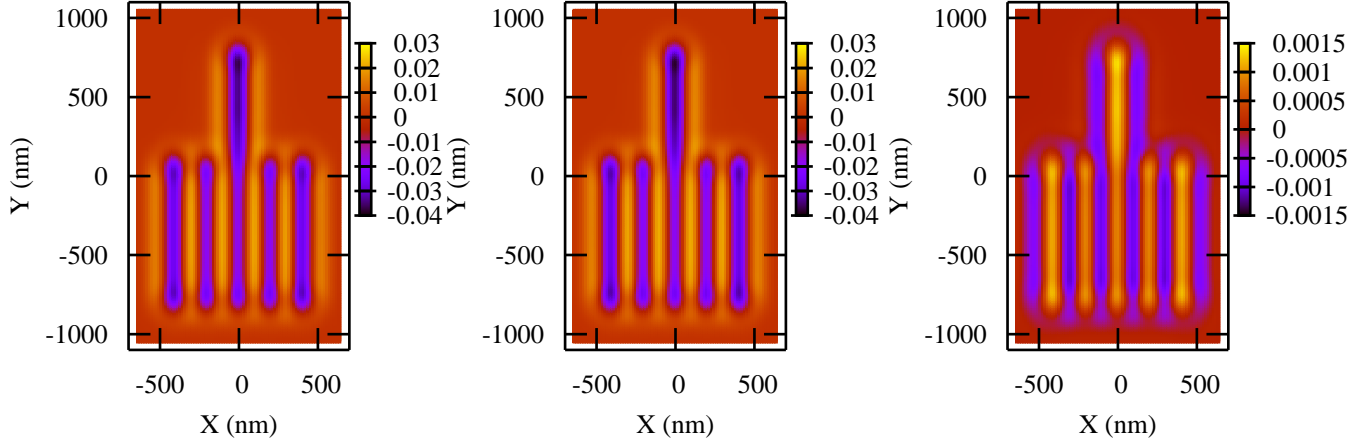
Table 1. Runtime comparison between I and $I_0 + I_2z^2$ (same number of kernels were used for I , I_0 and I_2).

Layout	I	$I_0 + I_2z^2$
fivebar	.19 sec	.38 sec
gate1	.16 sec	.34 sec
gate2	.18 sec	.35 sec

When aerial images at N ($N > 2$) different z values should be computed, it is obvious the second method is advantageous. The time complexity is $O(N)$ for the first method. However, the time complexity is $O(1)$ for the second method. So VLIM is fast enough to be used in OPC software to generate variational process data.

3.4. Comparison Between Two I_2 Calculation Methods

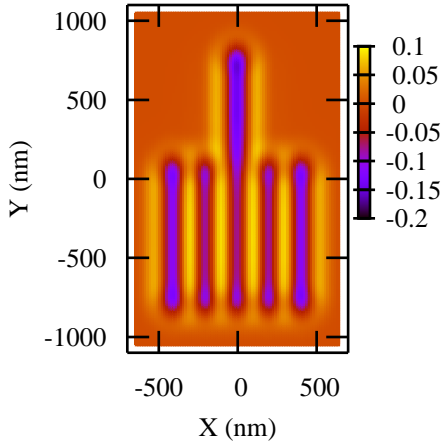
Since $I(x, y; z) \cong I_0(x, y) + I_2(x, y)z^2$ for small z , in addition to the direct I_2 calculation method in section 2, we can also compute $I_2(x, y)$ using $I_2(x, y) = \frac{I(x, y; z_0) - I(x, y; 0)}{z_0^2}$ with some specific small z_0 (the indirect I_2 calculation method). Denoting the error bounds of $I(x, y; z_0)$ and $I(x, y; 0)$ as $EB_{z_0}(m)$ and $EB_0(m)$ respectively, the error bound of $I_2(x, y)$ by the indirect method is $EB_{\text{indir}}(m) = \frac{EB_{z_0}(m) + EB_0(m)}{z_0^2}$, where m is the number of kernels



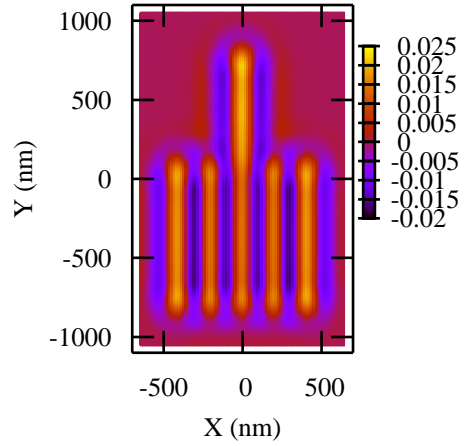
(a) $I|_{z=z_0} - I|_{z=0}$ image intensity map

(b) $I_2 z_0^2$ image intensity map

(c) $I_4 z_0^4$ image intensity map



(d) $I_2 z_1^2$ image intensity map



(e) $I_4 z_1^4$ image intensity map

Figure 4. $I|_{z=z_0} - I|_{z=0}$ and $I_2 z_0^2$ are almost the same. $I_2 z_0^2$ is about 20 times $I_4 z_0^4$. $I_2 z_1^2$ is about 5 times $I_4 z_1^4$. ($z_0 = 100\text{nm}$ and $z_1 = 200\text{nm}$)

used. Figure 5 shows I_2 error bounds of the two methods. The direct method is clearly better than the indirect method, because the former one has a smaller error bound than the latter one if the same number of kernels are used.

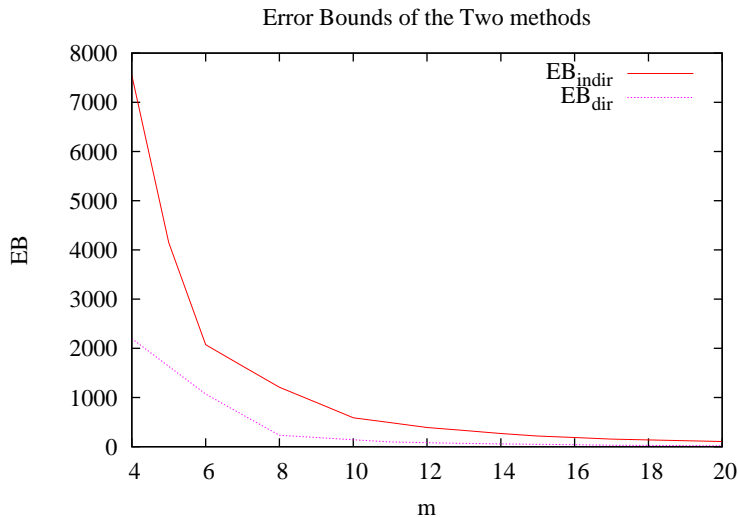


Figure 5. Error bounds of the two methods as a function of the number of kernels m ($z_0 = 50\text{nm}$). The other optics parameters are the same as those in section 3.1.

4. CONCLUSIONS

In this paper, an analytical defocus aerial image expansion method is derived. A variational lithography model is proposed, and its accuracy is verified with the industry standard PROLITHTM. The runtime of VLIM is comparable with traditional non-variational lithography model, but VLIM can compute FEM.

Current OPC software is unable to do full process window optimization since simulation over the process window is too slow. VLIM enables OPC software to overcome this barrier. Thus, a more robust layout may be generated.

ACKNOWLEDGMENTS

This work is partially sponsored by SRC, Fujitsu, IBM Faculty Award and Sun. We used computers donated by Intel Corporation and lithography simulation software (PROLITHTM) donated by KLA-Tencor.

REFERENCES

1. T. A. Brunner and R. A. Ferguson, "Approximate models for resist processing effects," in *Proc. SPIE 2726*, pp. 198–207, June 1996.
2. N. B. Cobb, A. Zakhor, and E. Miloslavsky, "Mathematical and CAD framework for proximity correction," in *Proc. SPIE 2726*, pp. 208–222, June 1996.
3. N. B. Cobb, A. Zakhor, M. Reihani, F. Jahansooz, and V. N. Raghavan, "Experimental results on optical proximity correction with variable-threshold resist model," in *Proc. SPIE 3051*, pp. 458–468, July 1997.
4. J. Randall, K. Ronse, T. Marschner, M. Goethals, and M. Ercken, "Variable-threshold resist models for lithography simulation," in *Proc. SPIE 3679*, pp. 176–182, July 1999.
5. Y. Granik, N. B. Cobb, and T. Do, "Universal process modeling with VTRE for OPC," in *Proc. SPIE 4691*, pp. 377–394, July 2002.
6. N. B. Cobb and Y. Granik, "OPC methods to improve image slope and process window," in *Proc. SPIE 5042*, pp. 116–125, 2003.

7. J. L. Sturtevant, J. A. Torres, J. Word, Y. Granik, and P. LaCour, "Considerations for the use of defocus models for OPC," in *Proc. SPIE 5756*, pp. 427–436, 2005.
8. Y. Granik and N. B. Cobb, "MEEF as a matrix," in *Proc. SPIE 4562*, pp. 980–991, 2002.
9. N. Cobb and Y. Granik, "New concepts in OPC," in *Proc. SPIE 5377*, pp. 680–690, 2004.
10. C. A. Mack, *Inside PROLITH: A Comprehensive Guide to Optical Lithography Simulation*, 1997.
11. D. Fuard, M. Besacier, and P. Schiavone, "Assessment of different simplified resist models," in *Proc. SPIE 4691*, pp. 1266–1277, 2002.
12. M. Born and E. Wolf, *Principles of Optics : Electromagnetic Theory of Propagation, Interference and Diffraction of Light*, 7 ed.
13. Y.-T. Wang, Y. C. Pati, and T. Kailath, "Depth of focus and the moment expansion," *OPTICS LETTERS* **20**, pp. 1841–1843, Sept. 1995.
14. J. Mitra, P. Yu, and D. Z. Pan, "RADAR: RET-aware detailed routing using fast lithography simulations," in *Proc. Design Automation Conference*, pp. 369–372, 2005.
15. Y. Pati, A. Ghazanfarian, and R. Pease, "Exploiting structure in fast aerial image computation for integrated circuit patterns," *IEEE Transactions on Semiconductor Manufacturing* **10**, pp. 62–74, Feb. 1997.
16. E. C. Kintner, "Method for the calculation of partially coherent imagery," *Applied Optics* **17**, pp. 2747–2753, Sept. 1978.